

Observation Capability of a Ground-Based Terahertz Radiometer for Vertical Profiles of Oxygen and Water Abundances in Martian Atmosphere

Takayoshi Yamada¹, Philippe Baron², Lori Neary³, Toshiyuki Nishibori, Richard Larsson, Takeshi Kuroda⁴, Frank Daerden⁵, and Yasuko Kasai

Abstract—We present the expected performance for a ground-based terahertz (THz) radiometer, a plan to be launched on the TERahertz EXplore-1 (TEREX-1) Mars exploration microspacecraft. The small THz passive radiometer has been developed for the TEREX series of future microspacecrafts. This spacecraft is an opportunity for organizations with limited resources and technology to conduct frequent missions to Mars well suited for resource exploration in contrast to all of the current and past Mars missions of large/giant class missions with fully government lead. The observation frequencies of the TEREX-1 radiometer are 474.64–475.64 and 486.64–487.64 GHz with a 100-kHz resolution, and the double-sideband noise temperature less than 3000 K. A theoretical error analysis is performed with the instrument characteristics to assess for the first time up-looking observations of atmospheric oxygen molecules (O₂) and water vapor (H₂O). Measurement errors for O₂ and H₂O are 7%–22% and 14%–25% with 8–17- and 5–10-km vertical resolution in the vertical ranges 0–55 and 0–25 km, respectively. TEREX-1 is also capable to measure minor species, O₃ and H₂O₂, with a precision better than 30% within two independent layers. We used the integration time of 1 h for all simulations. Our theoretical simulation showed the instrument characteristics of the TEREX-1 sensor are able to observe vertical profiles of O₂ and H₂O abundances with the same level of the large class missions.

Index Terms—Atmospheric observation, error analysis, lander, Mars, terahertz (THz).

Manuscript received May 4, 2021; revised July 30, 2021 and November 11, 2021; accepted February 13, 2022. Date of publication February 16, 2022; date of current version March 24, 2022. This work was supported in part by the Research and Development Program on Key Technology in Terahertz Frequency Bands, Ministry of Internal Affairs and Communications, under Grant JPJ000254; and in part by the Japan Society for the Promotion of Science (JSPS) KAKENHI under Grant 21K13985. (Corresponding author: Takayoshi Yamada.)

Takayoshi Yamada is with the Terahertz Technology Research Center, National Institute of Communication and Technology, Tokyo 184-8795, Japan (e-mail: yamada-takayoshi@nict.go.jp).

Philippe Baron is with the Department of Electrical, Electronics and Information and Communication Engineering, Osaka University, Osaka 565-0871, Japan (e-mail: philippe@eei.eng.osaka-u.ac.jp).

Lori Neary and Frank Daerden are with the Belgian Institute for Space Aeronomy, 1180 Brussels, Belgium (e-mail: lori.neary@aeronomie.be; frank.daerden@aeronomie.be).

Toshiyuki Nishibori is with the Japan Aerospace Exploration Agency, Tsukuba 305-8505, Japan (e-mail: nishibori.toshiyuki@jaxa.jp).

Richard Larsson is with the Max Planck Institute for Solar System Research, 37077 Göttingen, Germany (e-mail: larsson@mps.mpg.de).

Takeshi Kuroda is with the Department of Geophysics, Tohoku University, Miyagi 980-8578, Japan (e-mail: tkuroda@tohoku.ac.jp).

Yasuko Kasai is with the Terahertz Technology Research Center, National Institute of Communication and Technology, Tokyo 184-8795, Japan, and also with the Graduate School of Pure and Applied Sciences, Tsukuba University, Tsukuba 305-8577, Japan (e-mail: ykasai@nict.go.jp).

Digital Object Identifier 10.1109/TGRS.2022.3152271

I. INTRODUCTION

THE vertical profiles of molecular oxygen (O₂) and water vapor (H₂O) have important roles to understand the oxygen and water cycle on Mars (e.g. [1]–[4]). Especially, previous studies suggested that the vertical profiles of O₂ and H₂O at lower altitude is influenced by surface processes on Mars. The global distribution and seasonal variations of water vapor and clouds have been relatively well understood since the first detection in 1963 [5]. A perturbed vertical profile of water vapor below 30-km altitude, which was previously thought to be uniform, was suggested [2]. This is likely to be affected by a more complex Martian water environment near the surface than expected, and future observations at various seasons, locations, and times are needed to understand the heterogeneity up to 30 km especially the variability below 5 km [2]. Molecular oxygen in the Martian atmosphere has been measured by *in situ* instruments of a rover [6] and landers [7], by remote sensing on the Earth-orbiting satellite [8] and from ground-based telescopes on the Earth [9], [10]. The high signal-to-noise ratio spectral data of Herschel/Heterodyne Instrument for the Far-Infrared (HIFI) observations indicate a potential increase of O₂ concentration near the surface [8], although the O₂ has been considered to have a vertically constant profile of about 1400 ppmv. The low-altitude O₂ profile is a key for understanding the possible emission of O₂ from the surface and to assessing the oxidation capacity of the Martian atmosphere (oxidizing water vapor, methane, and various hydrogen radicals). However, the low-altitude O₂ and H₂O profiles have not been properly measured yet.

Remote sensing the submillimetre-wave range up to frequencies of approximately 5 terahertz (THz) was able to measure with the high-frequency resolution, individual rotational transitions of molecules in the thermal emission of atmospheres of the astrophysical targets. Previous observations using the submillimetre-wave range have been conducted by ground-based or Earth-orbiting satellite measurements for the study of Mars. Ground-based observations have mainly detected minor species using its high-frequency resolution and signal-to-noise ratio, rather than water and oxygen lines because they are absorbed by the Earth's atmosphere. The ground-based measurement have suggested upper limits of volatile gases, such as SO₂, SO, H₂S, and OCS by using disk-averaged spectra (e.g., [11]–[13]). The H₂O₂ observation

with the James Clerk Maxwell Telescope (JCMT) suggested that the observed amount, 18 ± 0.4 ppbv at 0–30 km of altitude, is three times larger than the upper limit level of the previous study [14]. The Submillimeter Wave Astronomy Satellite (SWAS) demonstrated high sensitivity of CO and H₂O observations and found a ~ 20 K drop in surface brightness temperature during a global dust storm [15], [16]. The Odin satellite provided constraints on the surface H₂O mixing ratios of $2 \times 3 \times 10^{-4}$ in disk-averaged spectrum [17]. Using Herschel/HIFI observations, Hartogh *et al.* [8] derived a constant volume mixing ratio (vmr) of 1400 ± 120 ppm for O₂ and determined upper limits of 2 ppb for H₂O₂. For further investigations, measurements from Mars-orbiting satellites are expected to improve the precision and the resolution and to expand the observation coverage of local time, vertical and spatial distributions, especially during dust events.

Space-born THz limb sounders orbiting Mars are under study to measure global vertical profiles of parameters, such as water vapor, oxygen molecules, carbon monoxide, trace gases (e.g., O₃ and H₂O₂), their isotopologues, winds, and temperature [18]–[21]. However, these projects have not been realized yet. Larsson *et al.* [21] proposed a limb and nadir submillimeter sensor under construction, named Terahertz Explore (TEREX) and a sensitivity study for the measurement of O₂, O₃, H₂O, and H₂O₂ vmrs and the wind speed and magnetic field strength. The estimated errors in 1-h nadir observation are approximately 1% from 10–40 km of altitude with about 20-km vertical resolution for O₂ and H₂O. It was decided that the realization of the TEREX orbiter comes after a lander mission due to the limitation of the amount of the propellant for the satellite thruster required for limb observations [22], [23].

The same TEREX, named TEREX-1, is now considered for ground-based observations on the Martian surface and will be the main payload of a lander under design [22], [23]. The lander is designed such that it can be constructed and operated by organizations with limited resources and technology, such as universities or emerging countries. Such observations will be complementary to those performed by Mars orbiters by providing continuous measurements over the same position. Compared with the satellite measurement [18]–[21], the ground-based measurement is less sensitive, especially for resolving the vertical profile of the atmospheric parameter. The advantage of ground-based observations is the possibility of increasing the observation time to improve the precision. TEREX-1 would be the first terahertz remote sensing instrument operating from the surface of a planet other than Earth, and this study is the first simulation study for such an instrument. The study aims at specifying the scientific value of this instrument by assessing the measurement errors, the vertical and time resolutions of the targeted molecules of O₂, H₂O, O₃, and H₂O₂.

The contents of this article are organized as follows. Section II provides an overview of TEREX-1, including the measurement method. In Section III, we describe the measurement simulation setup, including radiative transfer calculation, i.e., the forward model, retrieval error analysis, and parameters for these calculations. In Section IV, we present the results of

error analysis for the targeted molecules. Finally, in Section V, we summarize our main results and future implications.

II. TEREX-1

TEREX is the name of the series of future microsatellite missions to Mars. It is a microsatellite to realize frequent opportunities to go to Mars for resource exploration, such as O₂ and H₂O, as a piggyback spacecraft of another large Mars orbiter or lander [21]–[23]. As explained in Section I, the lander will be the first mission and subsequent will be orbiters [21]. The lander was conceptually designed for a novel, small, and simple Mars lander with simulations of the entry, descent, and landing processes, and a feasible thermal and power plan while conducting a THz sensor mission on the Martian surface [22], [23].

A. Instrument Description

Since the sensor is to be mounted on the microlander, it is expected to be light (<8 kg), small ($384 \times 384 \times 357$ mm³) and with a low-power budget (30 W). The instrument configuration is mostly inherited from the orbiter design [21], which was under development. The local oscillator changed from 484.15 to 481.14 GHz with a central intermediate frequency (IF) of 6 GHz due to the specification of a phase-locked dielectric resonator oscillator. It will operate in the double-sideband mode so that the measured radiation will be between 474.64–475.64 and 486.64–487.64 GHz, which includes absorption lines of O₂ at 487.25 GHz, H₂O at 474.69 GHz, H₂O₂ at 475.20 and 487.20 GHz, and O₃ at 487.35 GHz. As discussed in Larsson *et al.* [21], this frequency range is decided by the tradeoff between O₂ at the upper sideband and H₂O at the lower sideband frequency. After downconverted to the IF signals, the power level is amplified to turn this analog signal into a digital signal by a digital fast Fourier transform (FFT) spectrometer [24]. The system noise temperature is expected to be approximately 3000 K in the DSB mode. The frequency resolution is expected to be less than 100 kHz. The antenna is made of carbon fiber reinforced plastic, and its diameter is about 20 cm. The antenna design is also inherited from the original limb sounder, which is used to avoid sidelobe contamination due to surface emission. The observation time was supposed to be ~ 1 h during a day according to the power plan [22]. Further information related to TEREX-1 instrument, such as an optical system, including calibration loads and spectrometer can be found in Nakagawa *et al.* [24], [25].

B. Measurement Method

The sensor was originally developed for the orbiter system, although it was modified minimally to enable the observation by the lander system. Fig. 1 shows the optical paths when observing the atmosphere, the calibration hot load (T_h), and the subcalibration load (T_c). The backend is a dual-polarized receiver, but only one channel is used at a time. The second one will be a backup system. TEREX-1 will operate with an up-looking geometry with a single field-of-view (FOV).

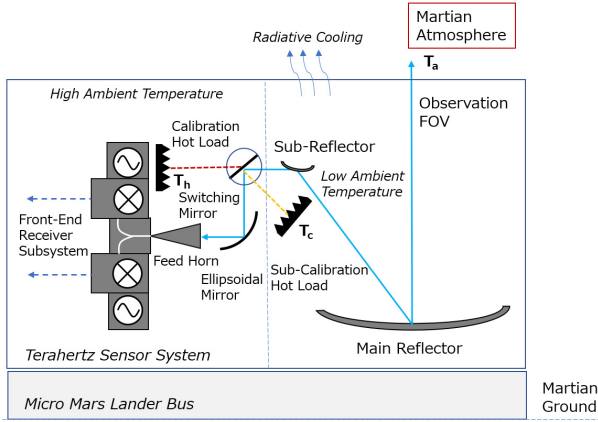


Fig. 1. Schematic of TEREX-1 calibration method. Blue line represents the optical path for atmospheric observation. Red and yellow dashed lines represent the optical path for the calibration hot and subhot loads, respectively, from the switching mirror.

The landing procedure is defined so that the antenna part faces the zenith to measure the atmosphere [22]. The precise antenna direction will depend on the attitude of the lander that will be derived from a three-axis accelerometer. The observation procedure uses a beam switching technique to calibrate the measured power. Unlike the original orbiter, the cold space cannot be used as the zero reference temperature. Calibration of the measured power will be performed using the hot and subcalibration loads whose temperatures will be monitored accurately. They are expected to be approximately 300 K and 235 K for T_h and T_c , owing to the internal heat generation of mission instruments and the exposure to the outside atmosphere (Fig. 1).

Typically, the raw power P measured with the radiometer is

$$P_i = G(T_{\text{sys}} + T_i) \quad (1)$$

where G is the radiometric gain, T_{sys} is the double-sideband system temperature, and T_i is the measured intensity expressed in the Rayleigh–Jeans temperature [26]. Note that these parameters are frequency dependent. The subscript i denotes the source of the signal, namely, a , h , or c , for atmosphere, hot, and subcalibration loads, respectively. The calibrated spectrum T_a is estimated by linear interpolation of the signals emitted by a hot and cold load

$$T_a = \frac{T_h - T_c}{P_h - P_c}(P_a - P_c) + T_c. \quad (2)$$

The random noise on the calibrated spectra is

$$\sigma_{n,T_a}^2 = \frac{1}{\Delta\nu\tau/4} \left(\frac{(T_a + T_{\text{sys}})^2}{2} + \frac{(T_c - T_a)^2}{(T_h - T_c)^2} (T_h + T_{\text{sys}})^2 + \frac{(T_a - T_h)^2}{(T_h - T_c)^2} (T_c + T_{\text{sys}})^2 \right) \quad (3)$$

where σ_{n,T_a} is the measurement noise, $\Delta\nu$ the frequency resolution, and τ the total observation time, including the integration of the atmospheric, hot, and cold loads spectra.

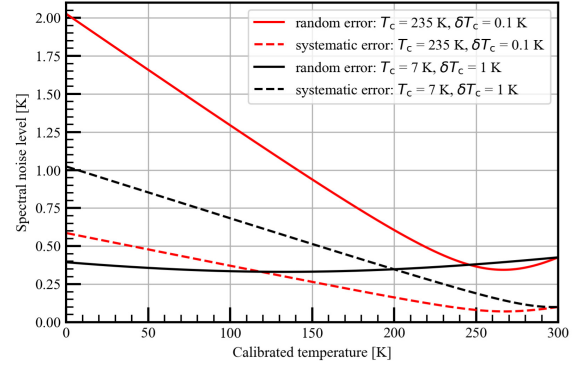


Fig. 2. Typical random (noise) and systematic (bias) errors on calibrated spectra with respect to T_a . Two scenario are shown: 1) $T_c = 235$ K and $\Delta T_c = 0.1$ K (red lines) and 2) $T_c = 7$ K and $\Delta T_c = 1$ K (black lines). Other parameters are $T_{\text{sys}} = 3000$ K, $T_h = 300$ K, $\delta T_h = 0.1$ K, $\Delta\nu = 100$ kHz, and $\tau = 1$ h.

This equation is derived from the radiometric equation

$$\delta T_i = \frac{T_{\text{sys}} + T_i}{\sqrt{\Delta\nu\tau_i}}, \quad \begin{cases} \tau_a = \frac{\tau}{2} & \text{for } i = a \\ \tau_h = \frac{\tau}{4} & \text{for } i = h \\ \tau_c = \frac{\tau}{4} & \text{for } i = c \end{cases} \quad (4)$$

where τ_a , τ_h , and τ_c are the integration times for observing atmosphere, hot load, and cold load, respectively.

A measurement bias can be induced by spectrally correlated uncertainties on the emission of the calibration signal intensity, such as errors induced by the load physical temperature. The bias σ_{b,T_a} can be derived as

$$\sigma_{b,T_a}^2 = \frac{(T_h - T_a)^2 \delta T_c^2 + (T_a - T_c)^2 \delta T_h^2}{(T_h - T_c)^2} \quad (5)$$

where δT_i is the uncertainty on the brightness temperature of the cold and hot loads.

Usually, the cold load is cold enough such that its brightness temperature has a value of the same order of magnitude as that of the atmospheric lines T_a . For the orbiter version of the instrument, the cosmic background at 2.7 K will be used. For TEREX-1, the temperature of both calibration loads will be significantly higher than T_a , and a proper strategy to calibrate the measurement needs to be defined based on laboratory studies. In particular, the radiometer nonlinearity and the spectral shape of the receiver temperature will be characterized with respect to the signal intensity. The results will be validated and constrained when the instrument operates on Mars using the spectral windows between the lines, typically between 5.5 and 5.9 GHz IF. This study is not within the scope of this article, and, here, we assume that the cold-spectrum represents a blackbody with a brightness temperature of approximately 7 K, namely, the atmospheric CO_2 continuum intensity. The retrieval errors will also be calculated for the case that the subcalibration load emission will be used as the cold spectrum ($T_c \sim 235$ K) to define a range that encompasses the actual retrieval performance.

Fig. 2 shows σ_{n,T_a} and σ_{b,T_a} with respect to T_a for both strategies. The method with $T_c \sim 7$ K is strongly influenced

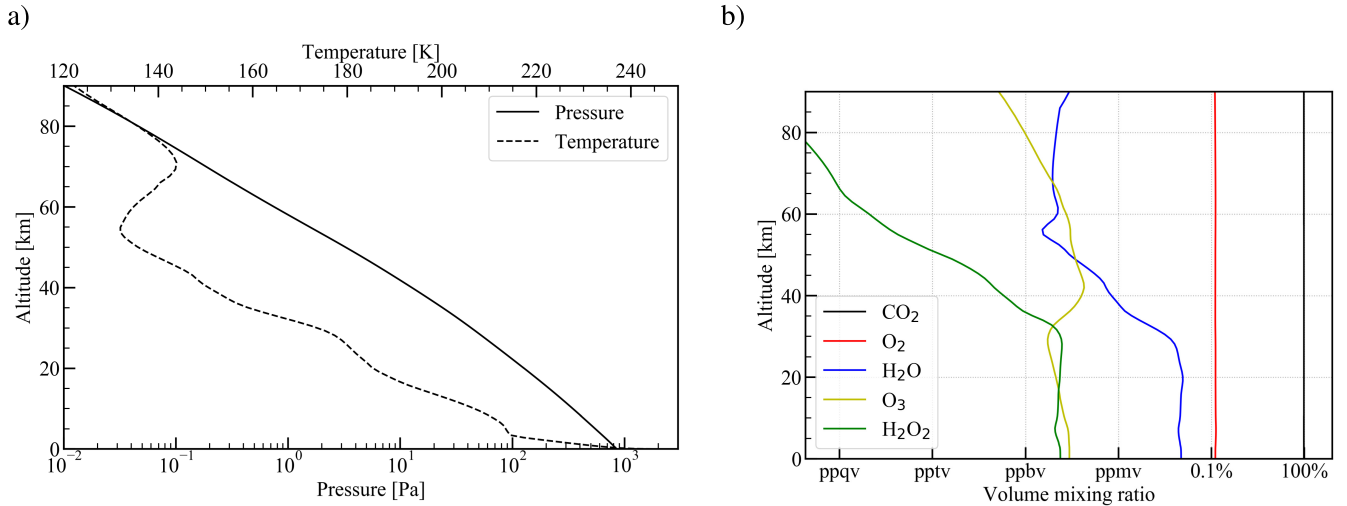


Fig. 3. Atmospheric conditions obtained from the 3-D general circulation model of the Martian atmosphere [1], [29] used in this study. (a) Vertical profiles of pressure (solid line) and temperature (dashed line) as true profiles in this study. (b) Vertical profiles of vmrs of CO₂ (black), O₂ (red), H₂O (blue), O₃ (yellow), and H₂O₂ (green).

by the level of CO₂ continuum emission intensity that is very uncertain for temperatures below 200 K [27], and atmospheric pressure and temperature. For this reason, the systematic error of the subcalibration brightness temperature is set to 1 K, a value much higher than the error induced by uncertainties on the physical temperature of the load. The latter uncertainty is set to 0.1 K. For $T_a = 10$ K, the random errors are 1.6 K and 0.27 K for methods 1 and 2, respectively. The differences on the systematic errors of these methods is insignificant (0.28 K and 0.78 K at $T_a = 10$ K).

III. MEASUREMENT SIMULATION SETUP

A. Forward Model

The signals by the TEREX-1 measurements were simulated by our radiative transfer model named Atmospheric Terahertz Radiative Transfer Simulator (ATRASU) [28]. This model performs line-by-line radiative transfer calculation [26] and we assume local thermodynamic equilibrium (LTE) in this study. The macroscopic radiative transfer equation can be expressed as

$$\frac{dI_v}{ds} = j_v - \alpha_v I_v \quad (6)$$

where I_v is the specific intensity [$\text{J m}^{-2} \text{sr}^{-1} \text{Hz}^{-1} \text{s}^{-1}$], j_v is the emission coefficient [$\text{J m}^{-3} \text{sr}^{-1} \text{Hz}^{-1} \text{s}^{-1}$], and α_v is the absorption coefficient [m^{-1}]. The intensity passing from s_0 (boundary condition of the path) to 0 (e.g., position of the sensor) along the path can be described by

$$I_v(0) = I_v(s_0) \exp(-\tau_v(s_0)) + \int_0^{s_0} j_v(s') \exp(-\tau_v(s')) ds' \quad (7)$$

where τ_v is the optical depth defined by $d\tau_v \equiv \sum \alpha_v ds$. The sum is performed over all active absorber contributions at the given frequency (nonoverlapping lines). For the targeted low altitudes, LTE is assumed as in previous studies [8], [17], [18], [20]. Therefore, the source function, $S \equiv j_v/\alpha_v$, is simply equal to the Planck blackbody radiation intensity. In this study, we use a pencil beam path without refraction for the line-of-sight and the Voigt line shape for α_v .

The atmospheric profiles for inputs were taken from a 3-D general circulation model of the Martian atmosphere [1], [29], as shown in Fig. 3. The solar longitude, landing position, and observation local time were assumed to be at 49°, 10.5 °N of latitude and 85.5 °E longitude, and noon, respectively, to be consistent with a previous study [22]. The measurement conditions follow the TEREX-1 measurement, i.e., the altitude is zero and the zenith angle is zero degrees.

Spectroscopic line parameters for the line-by-line calculation are taken from the high-resolution transmission (HITRAN) molecular absorption database (www.hitran.org) [30]. Moreover, broadening parameters for target lines were adapted to Martian conditions by using measured or calculated values for CO₂ broadening or, if measurements were not available, air-broadening parameters scaled by a factor of 1.65 as estimated from the ratio of collisional broadening coefficients in air and CO₂ for molecules and lines already studied by Urban *et al.* [18]. Collisional linewidth parameters of the H₂O broadened by CO₂ are taken from theoretical calculations [31].

Fig. 4 shows the simulated spectrum of TEREX-1 with estimated noise levels. The DSB spectrum is the sum of the half powers of the upper sideband spectrum and lower sideband spectrum on the IF range. There are 10000 channels due to 100-kHz frequency resolution to resolve the line shape. The estimated random noise level is less than 0.4 K. The signal heights at line center frequency for each molecule from the baseline are 14.1, 0.6, 98.1, and 0.6 K for O₂, O₃, H₂O, and H₂O₂, respectively.

B. Error Analysis

We follow the formalism of the “maximum *a posteriori* (MAP) solution” [32] which deals with the retrieval of unknown state \mathbf{x} related to a noisy measurement \mathbf{y} by forward model $\mathcal{F}(\mathbf{x}, \mathbf{b})$

$$\mathbf{y} = \mathcal{F}(\mathbf{x}, \mathbf{b}) + \boldsymbol{\epsilon}_y \quad (8)$$

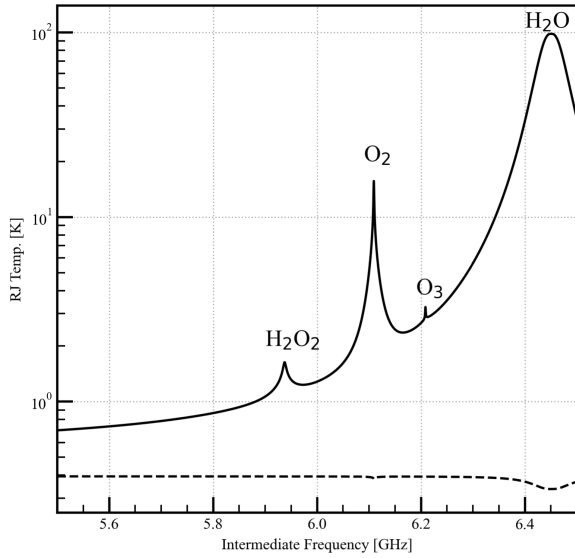


Fig. 4. Simulated spectrum (solid line) and 1-sigma noise level for 1-h integration (dashed line). Noise is assessed for the total observation time $\tau = 1$ h and system temperature $T_{\text{sys}} = 3000$ K. Noise level is estimated using the second calibration approach described in Section II-B.

where \mathbf{b} and $\boldsymbol{\epsilon}_y$ describe the forward model parameters and the measurement error, respectively. We use our radiative transfer model as the forward model. The MAP leads to the maximum likelihood solution, $\hat{\mathbf{x}}$, which minimizes the generalized χ^2

$$\chi^2 = [\mathbf{y} - \mathcal{F}(\mathbf{x}, \mathbf{b})]^T \mathbf{S}_y^{-1} [\mathbf{y} - \mathcal{F}(\mathbf{x}, \mathbf{b})] + (\mathbf{x} - \mathbf{x}_a)^T \mathbf{S}_x^{-1} (\mathbf{x} - \mathbf{x}_a) \quad (9)$$

where superscripts “ -1 ” and the “ T ” indicate the inverse and transpose of the matrix, respectively; \mathbf{x}_a , \mathbf{S}_x , and \mathbf{S}_y are an *a priori* knowledge of \mathbf{x} , the covariance matrix representing the natural variability of \mathbf{x} , and the covariance matrix representing the variability of the measurement error. The solution $\hat{\mathbf{x}}$ is calculated by finding the partial derivatives of χ^2 with respect to each element of \mathbf{x} when it becomes zero which is described as

$$\frac{\partial \chi^2}{\partial x(j)} = 0 \quad (10)$$

where $x(j)$ is the j th element of \mathbf{x} .

Solving (10) is not straightforward due to the nonlinearity of radiative transfer equation with respect to \mathbf{x} mostly for optically thick conditions. For the error analysis, we use the standard linear formalism which leads to the retrieved state, $\hat{\mathbf{x}}$

$$\hat{\mathbf{x}} = \mathbf{x}_a + \mathbf{D}(\mathbf{y} - \mathbf{K}\mathbf{x}_a) \quad (11)$$

where \mathbf{K} and \mathbf{D} are the matrices of weighting function and the contribution function described as

$$\mathbf{K} = \frac{\partial \mathbf{y}}{\partial \mathbf{x}} \quad (12)$$

and

$$\mathbf{D} = \frac{\partial \hat{\mathbf{x}}}{\partial \mathbf{y}} = (\mathbf{K}^T \mathbf{S}_y^{-1} \mathbf{K} + \mathbf{S}_x^{-1})^{-1} \mathbf{K}^T \mathbf{S}_y^{-1} \quad (13)$$

respectively.

The averaging kernel matrix $\mathbf{A} = \mathbf{D}\mathbf{K} = \partial \hat{\mathbf{x}} / \partial \mathbf{x}$ represents the sensitivity of the retrieved state with respect to the true state. The measurement response, $\mathbf{m}(i) = \sum_j \mathbf{A}(i, j)$, is useful to indicate the weight of the true state in the retrieved value at the altitude level i . We chose the altitude range where $\mathbf{m}(i)$ is higher than 0.7 as the good measurement response. The trace of \mathbf{A} gives the degrees of freedom for signal (DFSs), which indicates the number of distinct pieces of information in the retrieved profile. By using \mathbf{A} , (11) can be rewritten as

$$\hat{\mathbf{x}} = (\mathbf{I} - \mathbf{A})\mathbf{x}_a + \mathbf{A}\mathbf{x} + \mathbf{D}\boldsymbol{\epsilon}_y, \quad (14)$$

where \mathbf{I} is the identity matrix.

For simultaneous retrieval of several atmospheric profiles, such as some molecular species and temperature, the \mathbf{x} can be also represented as

$$\mathbf{x} = \begin{pmatrix} \mathbf{x}^1 \\ \vdots \\ \mathbf{x}^k \end{pmatrix} \quad (15)$$

in which \mathbf{x}^1 and \mathbf{x}^k are the state representing the vertical profiles of the first and k th profiles, respectively. Consequently, \mathbf{A} is rewritten in the following form:

$$\mathbf{A} = \begin{pmatrix} \mathbf{A}^{1,1} & \dots & \mathbf{A}^{1,k} \\ \vdots & \ddots & \vdots \\ \mathbf{A}^{k,1} & \dots & \mathbf{A}^{k,k} \end{pmatrix} \quad (16)$$

where $\mathbf{A}^{m,n} = \partial \hat{\mathbf{x}}^m / \partial \mathbf{x}^n$ with m th atmospheric profile and n th atmospheric profile.

The total error in the estimated profile results from the three components: 1) measurement noise errors $\boldsymbol{\epsilon}_y$; 2) the error on the *a priori* profile $\boldsymbol{\epsilon}_a$ meaning $\mathbf{x} - \mathbf{x}_a$; and 3) forward model parameter errors $\boldsymbol{\epsilon}_b$. The error in $\hat{\mathbf{x}}$ can be expressed by

$$\hat{\mathbf{x}} - \mathbf{x} = \mathbf{D}\boldsymbol{\epsilon}_y + (\mathbf{I} - \mathbf{A})\boldsymbol{\epsilon}_a + \mathbf{D}\mathbf{K}_b\boldsymbol{\epsilon}_b \quad (17)$$

where $\mathbf{K}_b = \partial \mathbf{y} / \partial \mathbf{b}$ representing the sensitivity of the calculated spectrum to the forward model parameters \mathbf{b} . Thus, the estimated covariance matrix of the retrieval can be separated into: 1) the measurement \mathbf{S}_M ; 2) smoothing error \mathbf{S}_A ; and 3) forward model parameter \mathbf{S}_B , defined as

$$\mathbf{S}_M = \mathbf{D}\mathbf{S}_y\mathbf{D}^T \quad (18)$$

$$\mathbf{S}_A = (\mathbf{A} - \mathbf{I})\mathbf{S}_a(\mathbf{A} - \mathbf{I})^T \quad (19)$$

$$\mathbf{S}_B = \mathbf{D}\mathbf{K}_b\mathbf{S}_b\mathbf{K}_b^T\mathbf{D}^T \quad (20)$$

where \mathbf{S}_a and \mathbf{S}_b are the covariance matrices associated with the a realistic *a priori* error and the forward model parameter error, respectively. In this study, we follow Baron *et al.* [33] for interpreting the blocks of \mathbf{S}_A (e.g., $\mathbf{S}_A^{m,n}$). The diagonal block elements represent the vertical resolutions, which include the effects of the smoothing errors. The nondiagonal blocks correspond to the contamination errors caused by the uncertainty of other atmospheric profiles. The covariance matrix corresponding to the contamination error of m th profile by n th profile changes, $\mathbf{S}_A^{m,n}$, is represented as $\mathbf{S}_A^{m,n} = \mathbf{A}^{m,n}\mathbf{S}_a^n(\mathbf{A}^{m,n})^T$, where \mathbf{S}_a^n is the *a priori* error of n th profile. Furthermore, as described in [34], we show the averaging kernel and full width of half maximum (FWHM) for each of its components

to evaluate the smoothing error instead of including this in the error budget.

C. Retrieval Conditions

The calibration of S_y takes into account the measurement noise for its diagonal elements. In this study, we take into account of 3 in which the parameters T_{sys} , T_h , T_c , δT_h , δT_c , $\Delta\nu$, and τ are 3000 K, 300 K, 7 K, 0.1 K, 1 K, 100 kHz, and 1 h, respectively. For more realistic estimation of S_y , the calibration uncertainty and measurement noise, including off-diagonal components will be published elsewhere.

The calculation of S_x takes into account *a priori* standard deviation, σ_x , at each vertical profile of 100% except for 30 K error for temperature profile with adjacent levels correlation. Then, S_x is considered as

$$S_x(i, j) = \sigma_x(i)\sigma_x(j) \exp\left(-\frac{|z(i) - z(j)|}{z_{\text{corr}}}\right) \quad (21)$$

where z and z_{corr} represent altitude grid and a distance correlation between i th and j th altitudes for the *a priori* parameter, respectively. We set z_{corr} to 10 km to defuse the constraint from the *a priori* value at one altitude to neighboring layers. The value of 10 km matches the typical resolution that is expected for the retrievals.

We set S_a and S_b for estimating the total error budget as follows. We consider an error of 50% with respect to the atmosphere for diagonal elements except for 15 K error for temperature profile, and correlations of 10 km [(21)] for S_a . The errors related to the forward model parameters include the uncertainty of antenna elevation and spectroscopic parameters. The uncertainty of the antenna direction depends on the accuracy of the three-axis accelerometer, and an arbitrary value of 0.025 degrees is chosen. The retrieved error calculated in this study can be scaled linearly to any pointing uncertainty we might assess in the future. Except for the H_2O broadening parameter, the spectroscopic parameters are taken from HITRAN [27], [30]. The uncertainties follow the higher values reported in the catalog. The H_2O broadening parameters are from Bauer *et al.* [31], and the uncertainty is arbitrary set to 5%.

We calculate K [(12)] by differentiation of the modeled signals with respect to the atmospheric vertical profiles. The state vector grid spacing for the error analysis is set to be 3 km. The absolute values of K scaled by x at each altitude for each profile are shown in Fig. 5. The scaled K values of O_2 , H_2O_2 , and O_3 have symmetric shapes about their center frequencies. The increase of the K values of O_3 above 30 km of altitude is caused by the strong increase of O_3 vmr, as shown in Fig. 3.

IV. RESULTS AND DISCUSSION

A. O_2

The measurement sensitivity to the O_2 profile is shown in Fig. 6 when the temperature is retrieved simultaneously. The scaled averaging kernel matrix, $A(i, j)x_a(j)/x_a(i)$ [33], and the measurement response are plotted on the left panel. The altitude range of the good measurement response is 0–55 km. The DFS is 4.9. The peak altitudes and FWHM of the scaled

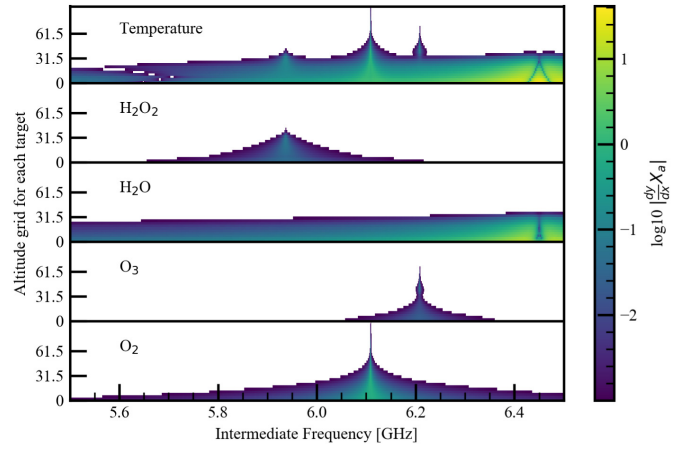


Fig. 5. Absolute scaled K value for each profile with respect to observation frequency and altitudes.

A for each altitude are also shown in Fig. 6. The FWHM is computed from the Gaussian fitting of A for each altitude. The peak altitudes show the most related altitudes of the retrieved state. The peak altitude of the averaging kernels is consistent with the retrieved altitude where the measurement response is good. The FWHM within the good measurement response is 8–17 km of altitude. The right-hand side panel of Fig. 6 shows the retrieval errors related to the *a priori* contamination, forward model parameters, and thermal noise error. The largest error component for O_2 retrieval is line parameter errors which are dominated by the 20% uncertainty of the O_2 line strength parameter. The error due to the uncertainty of the antenna direction is less than 0.0023%. Such an error remains negligible even if a pointing error 10 \times larger than that assumed in this study is considered. Most of the error from line parameters is regarded as systematic error. On the other hand, the noise and *a priori* contamination, including temperature profile errors, are random errors, which can be reduced by the observation integration time. Consequently, the random error for retrieving the O_2 profile is 7%–22% with the systematic error of 15%–27%.

The retrieval errors increase if we consider the calibration strategy for which the subcalibration load is used as the cold spectrum ($T_c \sim 235$ K). The spectral noise level increases from approximately 0.4 K to 2.0 K. The altitude range of the good measurement response is narrowed to 0–52 km. The peak altitude of the averaging kernels is consistent with the retrieved altitude below 40 km. The DFS decreases to 3.5. The FWHM increases by 1.2–1.4 \times compared with the calibration strategy using the atmospheric CO_2 continuum intensity as the cold spectrum ($T_c \sim 7$ K). The random error for retrieving the O_2 profile increases to 10%–28% with the systematic error of 15%–22%.

B. H_2O

The measurement sensitivity to the H_2O profile is shown in Fig. 7 when the temperature is retrieved simultaneously. The altitude range of the good measurement response is 0–25 km. The DFS is 3.5 and the FWHM within the good measurement response is 5–10 km of altitude. The random

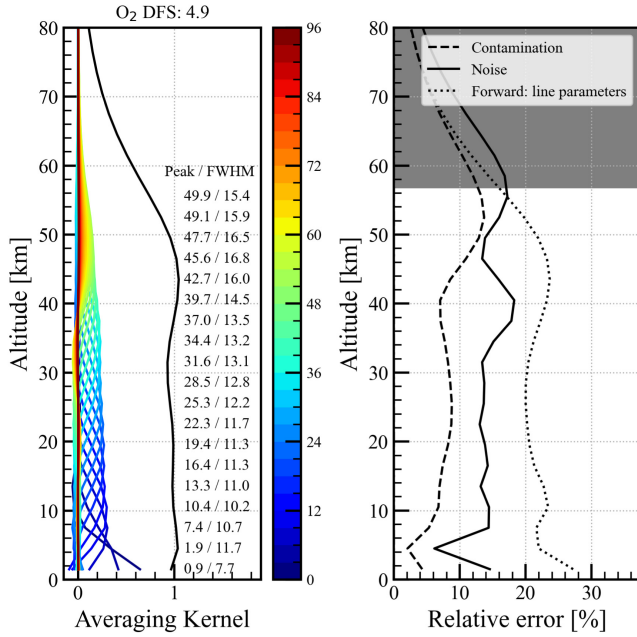


Fig. 6. O₂ retrieval by TEREX-1 up-looking with 1-h integration time observation and with simultaneous temperature retrieval. Left: Scaled averaging kernels of the retrieved O₂ profile for each altitude and measurement response (black line). The color bar shows the related altitude of the state of averaging kernels. DFS value is shown at the top of the panel. Peak altitude and FWHM values for each component of averaging kernels are shown on the right-hand side of the panel. Right: Expected retrieval errors. Dashed, dotted, and solid lines represent contamination error from the other profiles, forward model errors from spectroscopic parameters, and thermal noise error, respectively. The shaded area represents the altitude range where the measurement response is less than 0.7.

error for retrieving H₂O profile is 13–25% with the systematic error of 5%–17%. The main source of the systematic errors is the 20% uncertainty of broadening coefficient parameters for H₂O. The error due to the uncertainty of the antenna direction is less than 0.0036%. For H₂O \mathbf{K} , an optically thick condition that has no sensitivity owing to low transparency between an atmospheric layer and sensor, can be seen around the center frequency of H₂O, as shown in Fig. 5. This implies the information of the center frequency of H₂O only corresponds to the state near the surface, and there is no sensitivity to upper layer information. This causes a decrease in the observational sensitivity of the water vapor content of the upper atmosphere and an increase in the error due to the temperature profile because the line intensity at optically thick condition linearly depends on the temperature in the considered atmospheric layer.

We demonstrate error analysis without retrieving temperature profile which reduces the retrieved sensitivity to atmospheric species especially H₂O profile below an altitude of 30 km. Note that reliable information of the temperature profile is needed to retrieve the vmr profiles without retrieving temperature. If we average 25 1-h integrated spectra (25 Martian days), the uncertainty of the temperature profile reduces to be about 3 K, which allows us to avoid retrieval temperature. Two scenarios were considered for the error analysis. One is retrieving vertical profiles in vmrs of atmospheric constituents

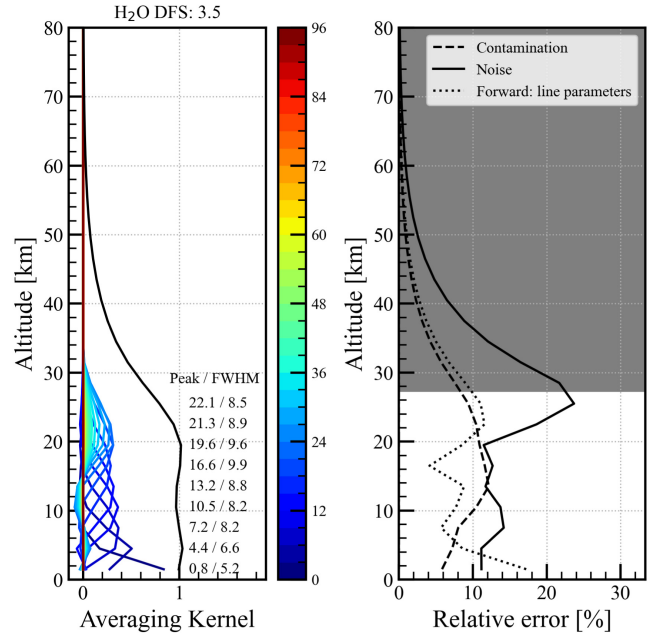


Fig. 7. Same manner as Fig. 6 but for H₂O profile.

from all the spectral ranges. The other is retrieving vertical profiles in vmrs of atmospheric constituents without optically thick frequency near the H₂O line. This condition sets the frequency range at which the information of \mathbf{K} is ignored in the retrieval procedure. For the frequency range, we consider optically thick frequency which has a transparency of radiations from surface to the top of the atmosphere of less than 0.2. The level of thermal noise in (13) is set to the same as that used for the 1-h integration time case. This allows us to get vmr retrievals with the DFS close to those obtained with temperature retrieval. In addition, the estimated retrieval error [(18)] due to the thermal noise will be divided by factor $5(\sqrt{25})$.

The left-hand side panel of Fig. 8 shows the results of an error analysis without temperature retrieval. The DFS for retrieving H₂O increased by 1.3 compared with the retrieval with temperature. The vertical resolution of H₂O profile becomes 1 km higher than that of the retrieval with temperature. However, the H₂O retrieval error from temperature uncertainty increases up to 130% because of the strong dependency of the H₂O line intensity on temperature. The random error, due to the contamination from other retrieved species and the measurement noise, is less than 5%. Consequently, this scenario is suitable if users are interested only in vmrs of H₂O and other species and can use a reliable temperature profile.

The right-hand side panel of Fig. 8 shows the results of the error analysis with the optically thick conditions. This condition ignores \mathbf{K} values at 6431.8–6469.6 MHz, which is an IF range that corresponds to the transparency less than 0.2. The DFS of the H₂O decreased to 3.0 with a decrease of the temperature uncertainty to 5%–21% due to the loss of the signal information around the H₂O centerline. The vertical resolution of H₂O profile becomes approximately 1 km

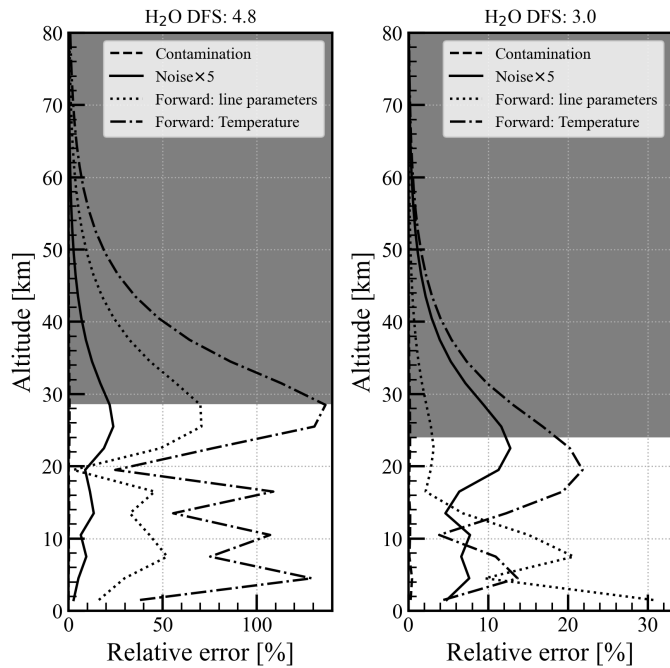


Fig. 8. Expected retrieval errors for H₂O without temperature retrieval when using the full-frequency range of TEREX-1 observation spectra (left) and ignoring optically thick frequency range (right) in the retrieval process. DFSs are shown at the top of each panel. Dashed, dotted, dash-dotted, and solid lines represent contamination error from the other profiles, forward model errors from spectroscopic parameters, forward model errors of temperature uncertainty, and thermal noise error multiplied by 5, respectively. The shaded area represents the altitude range where the measurement response is less than 0.7.

lower than that of the retrieval with temperature. This retrieval scenario allows us to not depend on a good knowledge of the temperature profile and reduce the contamination due to other retrieved species. This error assessment is based on an uncertainty of 3 K on the temperature profile which is questionable due to the lack of data. However, the error found in this study can be easily updated because it is linearly proportional to the assumed temperature error.

C. Temperature

As shown in Fig. 5, the sensitivity of temperatures below 30 km mostly originates from the H₂O spectrum. The transition from positive values to minus values occurs from the H₂O line frequency to its outer frequency region. The O₂ line also contributes to the temperature at the upper 30 km. Fig. 9 shows the measurement sensitivity to the temperature profile. The altitude range of the good measurement response is 0–15 km. The DFS is 2.8 and the FWHM within the good measurement response is 5–16 km of altitude. The random error for retrieving temperature profile is 2%–5% with the systematic error of 2%–3%. The main source of the systematic errors is the uncertainty of broadening coefficient parameters for H₂O.

D. Minor Species and Detection Limits

The atmospheric profiles of minor species, O₃ and H₂O₂, are also expected to be retrieved with approximately two-layer

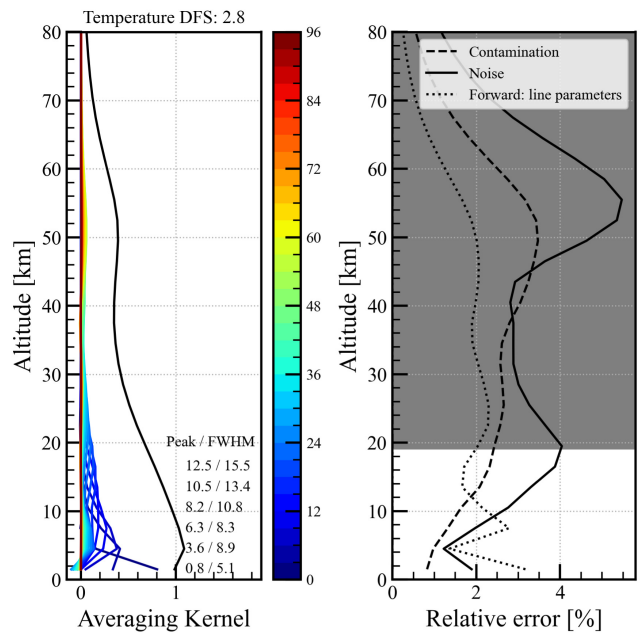


Fig. 9. Same manner as Fig. 6 but for temperature profile.

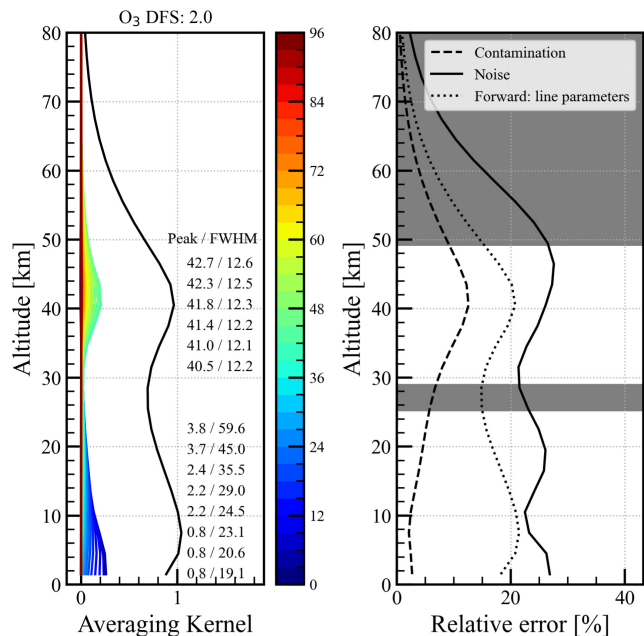


Fig. 10. Same manner as Fig. 6 but for O₃ profile.

vertical resolution. The measurement sensitivity to the O₃ profile is shown in Fig. 10. The peak altitudes of O₃ averaging kernels are not consistent with retrieved altitude and are 0–4 km for all averaging kernels peaking below 20 km and 40–43 km between for those peaking between 30–45 km, despite the good measurement response. TEREX-1 has the sensitivity to the O₃ profile at approximately 42-km altitude with about 13-km vertical resolution because of the strong increase of O₃ vmr above 30-km altitude. The random error for the O₃ profile is 22%–30% with 15%–22% of systematic errors. In the case of the H₂O₂, the altitude range of the good

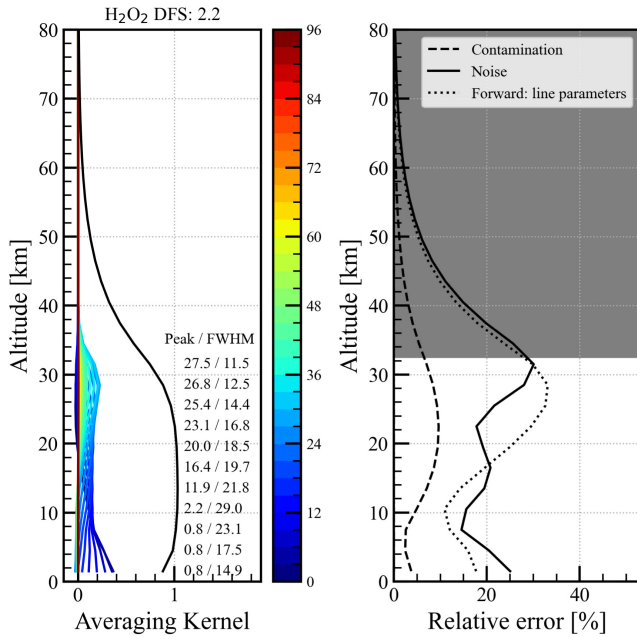


Fig. 11. Same manner as Fig. 6 but for H_2O_2 profile.

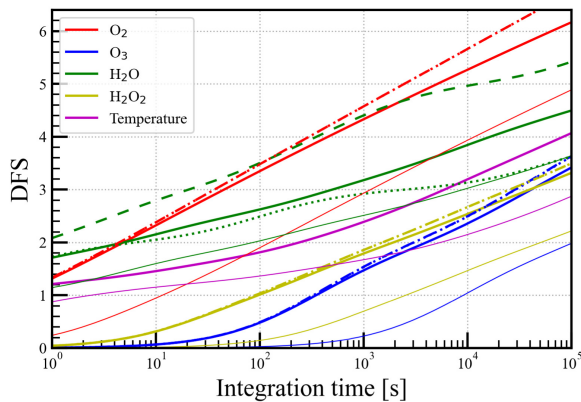


Fig. 12. DFS for each retrieving profile with temperature (solid), without temperature (dashed), and optically thick conditions (dotted). The DFSs are shown for the calibration case using $T_c \sim 7$ K cold spectrum. The DFSs for the calibration case using $T_c \sim 235$ K subcalibration load and temperature retrieval are shown with thin solid lines. Integration time includes those for the atmospheric, hot and cold loads spectra.

measurement response is 0–30 km with 12–30 km of FWHM, as shown in Fig. 11. The random error for H_2O profile is 14%–30% with 10%–34% of systematic errors, respectively.

We present the tradeoff between DFSs and integration time from one second to one day for both calibration scenarios in Fig. 12. The integration time to obtain at least a column layer profile of H_2O_2 and O_3 are 100 and 400 s, respectively, for the best calibration method. The retrieval scenario without temperature retrieval gives higher values of DFS for atmospheric constituents than the retrieval with the temperature profile, especially for a longer integration time. This implies a better signal-to-noise ratio of spectra has more information of temperature profile for each atmospheric constituent. The decrease of the DFS of H_2O with respect to the increase of the integration time for the optically thick

condition implies that a higher signal-to-noise ratio of H_2O spectra has more information about temperature and vmr profile around the surface altitude. An integration time of one second gives more than one DFS value for H_2O , O_2 , and temperature retrieval, i.e., at least a column layer can be retrieved from the measurement signal. For the calibration strategy for which subcalibration load is used as the cold spectrum, the required integration time is ten times longer to obtain similar results.

V. CONCLUSION

We studied the observation capability of the ground-based THz radiometer for vertical profiles of O_2 and H_2O in the Martian atmosphere. Considering the up-looking geometry and 1-h observation time, the expected measurement errors for O_2 and H_2O are 7%–22% and 14%–25% with 8–18- and 5–10-km vertical resolution in the vertical range 0–55 km and 0–25 km, respectively. The measurement error for temperature retrieval is 2%–5% with 5–16-km vertical resolution in the altitude range from 0 to 15 km. Scenarios without the retrieval of the temperature profile show improvements of the measurement error for H_2O profile in case of a large amount of H_2O vmr or reliable temperature profiles from other sources are available. Further investigations will be conducted on the use of ancillary information on the temperature profile. For instance, the error of 3 K could be obtained from proposed limb sounders [18], [21]. TEREX-1 is also capable to measure O_3 and H_2O_2 signals and retrieve vertical profiles in two independent layers with 30% measurement error. The minimum integration time to obtain at least one DFS values are <1, 400, <1, 100, <1 seconds for O_2 , O_3 , H_2O , H_2O_2 , and temperature profiles, respectively. These errors correspond to the best scenario for the calibration. If we consider the worst case scenario, namely, $T_c \sim 235$ K used as cold load spectrum, we found that the retrieval errors and DFS are degraded by about 20%–40% in the case of O_2 . The laboratory measurements of pressure broadening parameters in CO_2 gas are important for reducing systematic spectroscopic errors. Further laboratory study using two calibration loads is needed to assess the errors on the calibrated spectra and to define a more optimal calibration strategy. The error ranges and vertical resolutions of TEREX-1 will certainly improve past and current observations. We believe this unique dataset will allow us to better understand the source and sinks of oxygen and water vapor on the Martian surface and to go on with further innovations related to human activity on Mars.

REFERENCES

- [1] F. Daerden *et al.*, “Mars atmospheric chemistry simulations with the GEM-Mars general circulation model,” *Icarus*, vol. 326, pp. 197–224, Jul. 2019.
- [2] L. K. Tamppari and M. T. Lemmon, “Near-surface atmospheric water vapor enhancement at the Mars Phoenix Lander site,” *Icarus*, vol. 343, Jun. 2020, Art. no. 113624. [Online]. Available: <https://www.sciencedirect.com/science/article/pii/S0019103517304499>
- [3] R. T. Clancy *et al.*, “Vertical profiles of Mars $1.27 \mu\text{m}$ O_2 dayglow from MRO CRISM limb spectra: Seasonal/global behaviors, comparisons to LMDGCM simulations, and a global definition for Mars water vapor profiles,” *Icarus*, vol. 293, pp. 132–156, Sep. 2017. [Online]. Available: <https://www.sciencedirect.com/science/article/pii/S0019103516307217>

- [4] L. Maltagliati *et al.*, "Annual survey of water vapor vertical distribution and water-aerosol coupling in the Martian atmosphere observed by SPICAM/MEx solar occultations," *Icarus*, vol. 223, no. 2, pp. 942–962, Apr. 2013. [Online]. Available: <https://www.sciencedirect.com/science/article/pii/S0019103512005064>
- [5] R. A. Schorn, C. Farmer, and S. J. Little, "High-dispersion spectroscopic studies of Mars. III.: Preliminary results of 1968–1969 water-vapor studies," *Icarus*, vol. 11, no. 3, pp. 283–288, 1969. [Online]. Available: <https://www.sciencedirect.com/science/article/pii/0019103569900633>
- [6] P. R. Mahaffy *et al.*, "Abundance and isotopic composition of gases in the Martian atmosphere from the curiosity rover," *Science*, vol. 341, no. 6143, pp. 263–266, 2013. [Online]. Available: <https://science.sciencemag.org/content/341/6143/263>
- [7] T. Owen, K. Biemann, D. R. Rushneck, J. E. Biller, D. W. Howarth, and A. L. Laflour, "The composition of the atmosphere at the surface of Mars," *J. Geophys. Res.*, vol. 82, no. 28, pp. 4635–4639, Sep. 1977. [Online]. Available: <https://agupubs.onlinelibrary.wiley.com/doi/abs/10.1029/JS082i028p04635>
- [8] P. Hartogh *et al.*, "Herschel/HIFI observations of Mars: First detection of O₂ at submillimetre wavelengths and upper limits on HCl and H₂O₂," *Astron. & Astrophys.*, vol. 521, p. L49, Oct. 2010.
- [9] E. S. Barker, "Detection of molecular oxygen in the Martian atmosphere," *Nature*, vol. 238, no. 5365, pp. 447–448, Aug. 1972.
- [10] N. P. Carleton and W. A. Traub, "Detection of molecular oxygen on Mars," *Science*, vol. 177, no. 4053, pp. 988–992, Sep. 1972. [Online]. Available: <https://science.sciencemag.org/content/177/4053/988>
- [11] H. Nakagawa *et al.*, "Search of SO₂ in the Martian atmosphere by ground-based submillimeter observation," *Planet. Space Sci.*, vol. 57, nos. 14–15, pp. 2123–2127, Dec. 2009.
- [12] A. S. Khayat, G. L. Villanueva, M. J. Mumma, and A. T. Tokunaga, "A search for SO₂, H₂S and SO above Tharsis and Syrtis volcanic districts on Mars using ground-based high-resolution submillimeter spectroscopy," *Icarus*, vol. 253, pp. 130–141, Jun. 2015.
- [13] A. S. Khayat, G. L. Villanueva, M. J. Mumma, and A. T. Tokunaga, "A deep search for the release of volcanic gases on Mars using ground-based high-resolution infrared and submillimeter spectroscopy: Sensitive upper limits for OCS and SO₂," *Icarus*, vol. 296, pp. 1–14, Nov. 2017.
- [14] V. A. Krasnopolsky, G. L. Bjoraker, M. J. Mumma, and D. E. Jennings, "High-resolution spectroscopy of Mars at 3.7 and 8 μ m: A sensitive search for H₂O₂, H₂CO, HCl, and CH₄, and detection of HDO," *J. Geophys. Res., Planets*, vol. 102, no. E3, pp. 6525–6534, Mar. 1997.
- [15] M. Gurwell *et al.*, "Submillimeter wave astronomy satellite observations of the Martian atmosphere: Temperature and vertical distribution of water vapor," *Astrophys. J.*, vol. 539, no. 2, p. L143, 2000.
- [16] M. Gurwell, E. Bergin, G. Melnick, and V. Tolls, "Mars surface and atmospheric temperature during the 2001 global dust storm," *Icarus*, vol. 175, no. 1, pp. 23–31, May 2005.
- [17] N. Biver *et al.*, "Wide-band observations of the 557 GHz water line in Mars with Odin," *Astron. Astrophys.*, vol. 435, no. 2, pp. 765–772, May 2005.
- [18] J. Urban, K. Dassas, F. Forget, and P. Ricaud, "Retrieval of vertical constituents and temperature profiles from passive submillimeter wave limb observations of the Martian atmosphere: A feasibility study," *Appl. Opt.*, vol. 44, no. 12, pp. 2438–2455, Apr. 2005. [Online]. Available: <http://ao.osa.org/abstract.cfm?URI=ao-44-12-2438>
- [19] Y. Kasai *et al.*, "Overview of the Martian atmospheric submillimetre sounder FIRE," *Planet. Space Sci.*, vols. 63–64, pp. 62–82, Apr. 2012. [Online]. Available: <http://www.sciencedirect.com/science/article/pii/S0032063311003242>
- [20] W. G. Read *et al.*, "Retrieval of wind, temperature, water vapor and other trace constituents in the Martian atmosphere," *Planet. Space Sci.*, vol. 161, pp. 26–40, Oct. 2018. [Online]. Available: <https://www.sciencedirect.com/science/article/pii/S0032063317304105>
- [21] R. Larsson *et al.*, "Mars submillimeter sensor on microsatellite: Sensor feasibility study," *Geosci. Instrum., Methods Data Syst.*, vol. 7, no. 4, pp. 331–341, Dec. 2018. [Online]. Available: <https://gi.copernicus.org/articles/7/331/2018/>
- [22] R. Takahashi, R. Sakagami, A. Wachi, Y. Kasai, and S. Nakasuka, "The conceptual design of a novel, small and simple Mars Lander," in *Proc. IEEE Aerosp. Conf.*, Mar. 2018, pp. 1–10.
- [23] R. Sakagami *et al.*, "Integral design method for simple and small Mars Lander system using membrane aeroshell," *Acta Astronautica*, vol. 144, pp. 103–118, Mar. 2018.
- [24] M. Nakagawa *et al.*, "Development of a molecular assessment high-resolution observation spectrometer (MAHOS) for microsatellites," *IEEE J. Miniaturization Air Space Syst.*, early access, Jun. 30, 2021, doi: 10.1109/JMASS.2021.3093549.
- [25] M. Nakagawa *et al.*, "Compact 480-GHz radiometer calibration unit with specular reflection absorber for atmospheric remote sensor on-board microsatellite," *IEEE Trans. THz Sci. Technol.*, vol. 11, no. 5, pp. 486–494, Sep. 2021.
- [26] J. Urban *et al.*, "Moliere (v5): A versatile forward- and inversion model for the millimeter and sub-millimeter wavelength range," *J. Quant. Spectrosc. Radiat. Transf.*, vol. 83, nos. 3–4, pp. 529–554, Feb. 2004.
- [27] T. Karman *et al.*, "Update of the HITRAN collision-induced absorption section," *Icarus*, vol. 328, pp. 160–175, Aug. 2019. [Online]. Available: <http://www.sciencedirect.com/science/article/pii/S0019103518306997>
- [28] T. Yamada, L. Rezac, R. Larsson, P. Hartogh, N. Yoshida, and Y. Kasai, "Solving non-LTE problems in rotational transitions using the Gauss–Seidel method and its implementation in the atmospheric radiative transfer simulator," *Astron. Astrophys.*, vol. 619, p. A181, Nov. 2018.
- [29] L. Neary and F. Daerden, "The GEM-Mars general circulation model for Mars: Description and evaluation," *Icarus*, vol. 300, pp. 458–476, Jan. 2018. [Online]. Available: <http://www.sciencedirect.com/science/article/pii/S0019103517302270>
- [30] I. E. Gordon *et al.*, "The HITRAN2016 molecular spectroscopic database," *J. Quant. Spectrosc. Radiat. Transf.*, vol. 203, pp. 3–69, Dec. 2017. [Online]. Available: <http://www.sciencedirect.com/science/article/pii/S0022407317301073>
- [31] A. Bauer, M. Godon, J. Carlier, and R. R. Gamache, "Absorption of a H₂O–CO₂ mixture in the atmospheric window at 239 GHz; H₂O–CO₂ linewidths and continuum," *J. Mol. Spectrosc.*, vol. 176, no. 1, pp. 45–57, Mar. 1996. [Online]. Available: <http://www.sciencedirect.com/science/article/pii/S0022285296900600>
- [32] C. D. Rodgers, *Inverse Methods for Atmospheric Sounding*. Singapore: World Scientific, 2000. [Online]. Available: <https://www.worldscientific.com/doi/abs/10.1142/3171>
- [33] P. Baron *et al.*, "Studies for the Odin sub-millimetre radiometer. II. Retrieval methodology," *Can. J. Phys.*, vol. 80, no. 4, pp. 341–356, Mar. 2002, doi: 10.1139/p01-150.
- [34] T. von Clarmann *et al.*, "Overview: Estimating and reporting uncertainties in remotely sensed atmospheric composition and temperature," *Atmos. Meas. Techn.*, vol. 13, no. 8, pp. 4393–4436, Aug. 2020. [Online]. Available: <https://amt.copernicus.org/articles/13/4393/2020/>



Takayoshi Yamada received the Ph.D. degree in science by developing a submillimeter radiative transfer simulator, including rotational non-LTE model and data analysis of remote sensing from Tokyo Institute of Technology, Tokyo, Japan, in 2018.

He is currently a Researcher with the National Institute of Information and Communications Technology, Tokyo. His scientific research interests include terahertz radiative transfer modeling and remote sensing for Earth's and planetary atmosphere.

Philippe Baron received the Ph.D. degree in physics from the University of Bordeaux, Bordeaux, France, in 1999.

He is currently with Osaka University, Osaka, Japan. His research interest includes atmospheric remote sensing with passive and active sensors.



Lori Neary received the Ph.D. degree in modeling deep convection, clouds and atmospheric chemistry from York University, Toronto, ON, Canada, in 2011.

She is currently a Research Scientist with the Royal Belgian Institute for Space Aeronomy, Brussels, Belgium. She is involved in the development of the GEM-Mars model. She is also a Co-Investigator of the NOMAD instrument onboard the ExoMars Trace Gas Orbiter. Her scientific focus is on numerical modeling of physical and chemical processes in the atmosphere of Mars.



Toshiyuki Nishibori received the D.E. degree in electrical and electronics engineering from Sophia University, Tokyo, Japan, in 1995.

From 1987 to 1992, he was with Ishikawajima Harima Heavy Industries Company, Ltd., Tokyo. From 1995 to 1998, he was a Lecturer with the Tokyo Metropolitan College of Aeronautical Engineering, Tokyo. In 1998, he joined the National Space Development Agency of Japan, Tokyo, where he is currently involved in the research and development of the Superconducting Submillimeter-Wave

Limb-Emission Sounder to be aboard the Japanese Experiment Module of the International Space Station for observing stratospheric minor constituents related to ozone depletion. Since 2015, he has been the Senior Researcher of Sensor System Research Group, Research and Development Directorate, Japan Aerospace Exploration Agency, Tsukuba, Japan. His research interests include antenna design and measurements at frequency submillimeter-wave region, quasi-optics, radar remote sensing, and ground-penetrating radars.



Takeshi Kuroda received the Ph.D. degree in general circulation modeling of Mars atmosphere from The University of Tokyo, Tokyo, Japan, in 2006.

He was with the Max Planck Institute for Solar System Research, Göttingen, Germany, Institute of Space and Astronautical Science, Japan Aerospace Exploration Agency, Tsukuba, Japan, and the National Institute of Information and Communications Technology, Tokyo, for the investigations of atmospheric Dynamics, RAdiation, MAterial Transport and their mutual InteraCtions of Mars (present and paleo), Jupiter, Venus, and beyond with the method of general circulation modeling. He is currently an Assistant Professor with the Department of Geophysics, Tohoku University, Sendai, Japan. He also joined the science teams of Akatsuki, Mars Atmosphere and Volatile Evolution (MAVEN), JUPiter ICy Moons Explorer (JUICE), and Martian Moons eXploration (MMX), and leads the scientific discussions of microsatellite terahertz Mars mission series TEREX. He is interested in the atmospheric environmental evolutions and habitability of planets and satellites and contributions to future manned explorations of Mars.



Richard Larsson received the Ph.D. degree in space engineering with a focus on studies about the Zeeman effect in planetary atmospheres from Luleå University of Technology, Luleå, Sweden, in 2016.

He is a Post-Doctoral Researcher with the Max Planck Institute for Solar System Research (MPS), Göttingen, Germany, where he is involved in the upcoming Jupiter Icy Moons Submillimetre Wave Instrument and operating MPS ground-based radiometers. His research interests include improving radiative transfer modeling techniques (modeling) and applying these techniques to better understand planetary atmospheres (retrieval).



Frank Daerden received the Ph.D. degree from Hasselt University, Hasselt, Belgium, in 2001.

He is currently a Senior Scientist with the Royal Belgian Institute for Space Aeronomy, Brussels, Belgium. He is also the Instrument Scientist for the NOMAD spectrometer suite on the ExoMars Trace Gas Orbiter. His expertise is 3-D global modeling of the atmosphere of Mars, with a focus on clouds and atmospheric chemistry. He co-develops the GEM-Mars model.



Yasuko Kasai received the Ph.D. degree in microwave molecular spectroscopy and radio astronomical observations from the Department of Chemistry, Tokyo Institute of Technology, Tokyo, Japan, in 1995.

She is currently an Executive Researcher with the National Institute of Information and Communications Technology, Tokyo. Her scientific research interest includes satellite remote sensing for Earth's and planetary atmosphere.